

LPSNet: End-to-End Human Pose and Shape Estimation with Lensless Imaging

Haoyang Ge^{1,†}, Qiao Feng^{1,†}, Hailong Jia¹, Xiongzheng Li¹, Xiangjun Yin¹, You Zhou², Jingyu Yang¹, Kun Li^{1,*}

¹Tianjin University, China ²Nanjing University, China

{ghy0623, fengqiao, jhl, lxz, yinxiangjun, yjy, lik}@tju.edu.cn zhouyou@nju.edu.cn

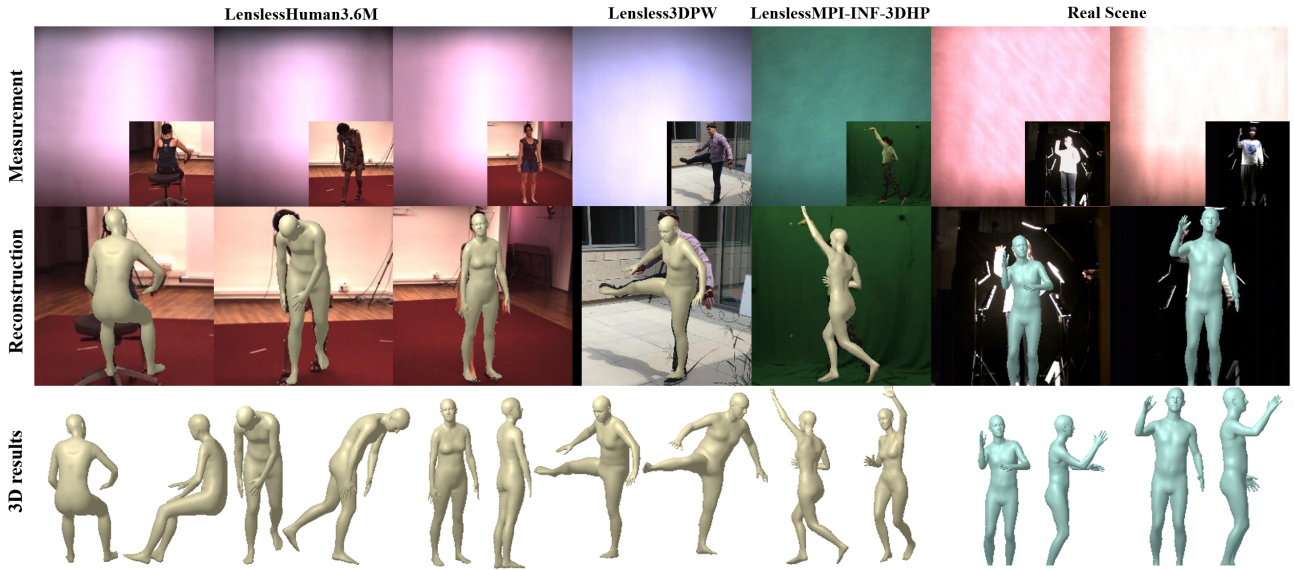


Figure 1. **LPSNet: End-to-End Human Pose and Shape Estimation with Lensless Imaging.** We contribute a framework for estimating human poses and shapes from individual lensless measurements. The first row shows the input measurements acquired by our lensless imaging system, the second row shows the estimated human poses and shapes from lensless measurements, and the bottom row shows the 3D results shown in different views.

Abstract

Human pose and shape (HPS) estimation with lensless imaging is not only beneficial to privacy protection but also can be used in covert surveillance scenarios due to the small size and simple structure of this device. However, this task presents significant challenges due to the inherent ambiguity of the captured measurements and lacks effective methods for directly estimating human pose and shape from lensless data. In this paper, we propose the first end-to-end framework to recover 3D human poses and shapes from lensless measurements to our knowledge. We specifically design a multi-scale lensless feature decoder to decode the lensless measurements through the optically encoded mask

for efficient feature extraction. We also propose a double-head auxiliary supervision mechanism to improve the estimation accuracy of human limb ends. Besides, we establish a lensless imaging system and verify the effectiveness of our method on various datasets acquired by our lensless imaging system. The code and dataset are available at <https://cic.tju.edu.cn/faculty/likun/projects/LPSNet>.

1. Introduction

In recent years, lensless imaging technologies [6, 7, 21, 27] have advanced significantly due to their many advantages, such as privacy protection, smaller size, simple structure, and lower cost. 3D human pose and shape (HPS) estimation [11, 16, 36, 37] requires miniaturized and

† Equal contribution.

* Corresponding author.

lightweight imaging system as application scenarios become more diverse. All these advantages, especially privacy, make the lensless imaging system very suitable as an imaging device for human pose and shape estimation. In this work, we propose LPSNet, which aims to estimate 3D human pose and shape from lensless measurements instead of RGB images, achieving cheaper and privacy-protecting 3D human pose and shape estimation.

A thin, lightweight, and potentially cost-effective optical encoder is used in a lensless imaging system instead of traditional cameras with lenses, while others are expensive, rigid, and occupy more space. At this stage, the application of a lensless imaging system is extensive, it is mainly used in the field of microscopic imaging, RGB image reconstruction, and so on. More valuable information can be obtained from lensless measurements due to the special optical encoding method of lensless imaging systems. Directly estimating human pose and shape from lensless measurements is not currently possible. The first step is to reconstruct an RGB image from a lensless measurement and then estimate the human pose and shape from the RGB images. However, experimental findings indicate that the reconstructed RGB images are of suboptimal quality, resulting in incomplete local features and significant deviations in the position of the human body. Combining these factors leads to inaccurate human pose estimation when using lensless measurements to reconstruct RGB images. This approach has computational burden and computational resources, making it very unfavorable for deployment at the endpoint.

In this paper, We aim to advance human pose and shape estimation using a lensless imaging system, which needs to overcome two main challenges. First, how to extract features from lensless measurements for human pose and shape estimation. Secondly, during early experiments, when using features extracted from lensless measurements to estimate human pose and shape, we found poor estimation accuracy of human limbs.

To address these challenges, we introduce LPSNet, the first end-to-end human pose and shape estimation framework with lensless imaging. To extract features from optically encoded lensless measurements, we propose a multi-scale lensless feature decoder (MSFDecoder). Specifically, we introduce a global perception layer to enhance the global decoding capability of MSFDecoder. The global information that has been optically encoded to the global can be efficiently decoded to obtain a feature map that can be used in subsequent processes. To improve pose and shape estimation, we propose a Double-Head Auxiliary Supervision(DHAS) mechanism to be implemented during training. Auxiliary supervision can improve the estimation accuracy of human limbs and correct results with large deviations.

Our main contributions can be summarized as follows:

- 1) We propose LPSNet, an end-to-end pose and shape esti-

mation network for lensless imaging systems. This is the first work to estimate human poses and shapes directly from lensless measurements.

- 2) We propose MSFDecoder, a Multi-Scale Lensless Feature Decoder that decodes and extracts features from lensless measurements, which can be receptive to global features in lensless measurements.
- 3) We propose a Double-Head Auxiliary Supervision mechanism for both pose and shape estimation, which can improve the estimation accuracy of human limbs.

2. Related Work

2.1. Lensless Imaging System

A conventional photographic camera typically comprises a focusing lens, which may consist of one or more optical elements and an image sensor positioned at or near the focal length of the lens. The lens in such a camera directs the projected light from the observed scene onto the sensor, aiming to accurately map specific scene points to individual pixels on the sensor. Conversely, in a lensless imaging system, the absence of a lens defines its configuration. Instead, an optical modulator, such as a coded amplitude mask or a diffuser, is positioned between the scene and the image sensor, often close to the sensor itself. As a result, the recorded data deviates significantly from the expected RGB image during imaging. In this process, the local information of the object transforms overlapping global information through the optically encoded mask.

Within the mask-modulated lensless systems, a fixed optical mask is introduced to create a versatile lensless system that can work for a wide range of object distances and lighting scenarios, whether passive or uncontrolled. The mask modulates the incoming light and generates a measurement that can be decoded through computational methodologies. Mask-modulated lensless imaging systems were used to perform 2D imaging [4, 7, 21], refocusing [7], 3D imaging [2, 7], and microscopic imaging [1, 2, 7].

Generally speaking, amplitude modulators and phase modulators [1, 4] are the two types of optical masks used in lensless imaging systems. Phase modulators can be further sub-categorized into phase gratings [32, 33], diffusers [2], and phase masks [7]. One key characteristic of a mask-modulated lensless system is the pattern the mask produces on the sensor for a point light source in the scene. We call this pattern the Point-Spread Function(PSF), and its properties determine the imaging model of the system. As shown in Fig. 2, we design a simple mask-modulated lensless system for data acquisition in this experiment. The lensless imaging system designed in our experiments chose a diffuser as the mask.

The main advantages of lensless imaging are as follows: lensless is small in size and can be assembled in a variety of

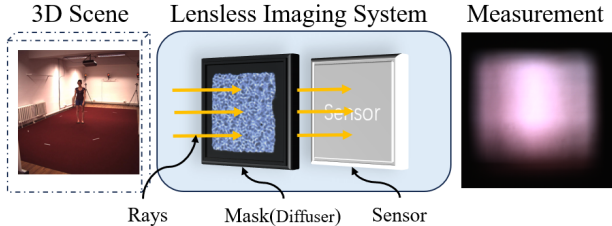


Figure 2. The workflow of the lensless imaging system and the final measurement obtained is the result obtained from the encoding of 3D scene information by the lensless imaging system. The optically encoded mask transforms local information in the 3D scene into overlapping global information.

miniaturized equipment; lensless is light and easy to carry; lensless cameras are still cheap to make; lensless cameras have a wide view field, larger than traditional wide-angle cameras; It can also protect the user’s privacy to a great extent.

2.2. Human Pose and Shape Recovery

There are two primary methods for human pose and shape estimation: optimization-based approaches and regression-based approaches. Numerous methodologies have been developed to estimate the three-dimensional human pose and shape by employing iterative optimization techniques, e.g., SMPLify [5] and variations of the SMPLify [22, 28, 31, 35].

Many existing Regression-based methods follow the architecture of HMR [16], which uses a pre-trained backbone to extract image features followed by regression to obtain SMPL [5] parameters. Many improvements to the original method have been proposed since its introduction. In particular, many papers have proposed alternative methods for pseudo-ground truth generation, including using temporal information [3], multiple views [23], or iterative optimization [15, 19, 29]. SPIN [19] proposed an in-the-loop optimization that incorporated SMPLify [5] in the HMR training, which combines the optimization-based approach and the regression-based approach for human pose and shape estimation. PyMAF [37, 38] proposes a pyramidal mesh alignment feedback loop for regression of SMPL parameters. Our approach references the design of PyMAF in the part of the SMPL parameters regression. PARE [18] proposes a body-part-guided attention mechanism for better occlusion handling. HKMR [10] performs a prediction guided by the hierarchical structure of SMPL. HMR2.0 [11] employs a large training dataset and proposes a fully transformer-based approach for 3D human pose and shape estimation from a single image. Many related approaches make non-parametric predictions, i.e., instead of estimating the parameters of the SMPL model, they explicitly regress the vertices of the mesh. GraphCMR [20] uses a

graph neural network for the prediction, METRO [25] and FastMETRO [8] use a transformer, while Mesh Graphomer [26] adopts a hybrid between the two.

In this paper, we propose the first work to perform end-to-end human pose and shape estimation from lensless measurements. We designed a multi-scale lensless feature decoder to decode the lensless measurements based on a mask-encoder to obtain more efficient features. We also propose a double auxiliary supervision mechanism to improve the estimation accuracy of human limbs.

3. Method

3.1. Overview

Our work focuses on human pose and shape estimation from lensless measurements. In this section, we present the technical details of our approach. As depicted in Fig. 3, the core of our method involves the following three components: 1) a Multi-Scale Lensless Feature Decoder(MSFDecoder) (Sec. 3.2) that can effectively decode the information encoded by the lensless imaging system; 2) a human parametric model regressor (Sec. 3.3) that takes the multi-scale features produced by MSFDecoder as input and predicts the SMPL parameters; 3) a Double-Head Auxiliary Supervision mechanism(DHAS) (Sec. 3.4) that can assist the LPSNet to improve the estimation accuracy of human limbs.

3.2. Multi-Scale Lensless Feature Decoder

As illustrated in Fig. 2, the optical information of the subject is diffused by the mask and projected onto the sensor. The process of obtaining measurements through the lensless imaging system can be treated as encoding optical information in the scene into lensless measurements. The goal of our lensless feature decoder D_M is to decode these lensless measurements to multi-scale features, which are then utilized for subsequent human body prediction. The design of the global perception layer G_P is inspired by HRNet [34]. The global perception layer inherits many of the advantages of HRNet [34] and can always maintain a high resolution, while the information interaction between different branches complements the information loss caused by the reduction in the number of channels. These advantages are important for extracting features from lensless measurements. Then, we design different convolutional layers for different scales of features that are used to refine the features.

Formally, the decoder takes a lensless measurement M as input and decodes the information encoded by the lensless imaging system. The global perception layer ensures the integrity of global information for each pixel by maintaining the high-resolution convolution branch and the low-resolution convolution branch in parallel. It further en-

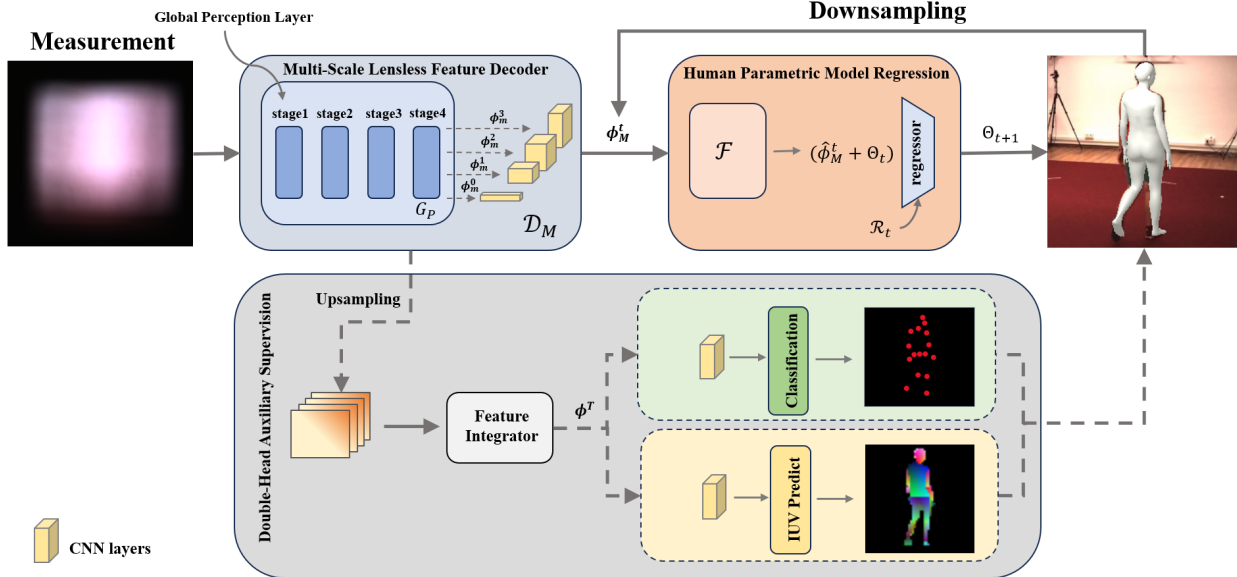


Figure 3. Overview of the proposed framework. A measurement M is passed through a Multi-Scale Lensless Feature Decoder to get spatial characteristics at different scales. These feature maps are fed into the regressor for human pose and shape estimation. Also, these feature maps are fed into the Double-Head Auxiliary Supervision to improve the estimation accuracy.

hances the information extraction accuracy by repeating the multi-scale fusion across parallel convolutions. As shown in Fig. 3, the global perception layer takes M as input and generates a set of multi-scale spatial features $\phi_m^{t=0,1,2,3}$ as input for the subsequent steps. The final output ϕ_M^t of the decoder is obtained by passing ϕ_m^t into different convolutional layers,

$$\phi_M^t = D_M(M). \quad (1)$$

With different scales of decoding, we can obtain feature maps at different granularities, through which we can perceive the location of people in the scene. The results obtained by the lensless decoder are utilized for subsequent predictions with the SMPL model, incorporating pose, shape, and camera parameters $\Theta = \{\theta, \beta, \tilde{\pi}\}$, where $\tilde{\pi}$ is pseudo-camera parameters for the subsequent projection calculation.

3.3. Human Parametric Model Regression

Our human parametric model regression is mainly inspired by the improved Human Mesh Regression described in PyMAF [37]. Different from the pyramid features obtained by deconvolution in PyMAF [37], our global perception layer exploits HRNet [16] to maintain more high-resolution information. We use a set of sampling points S_t and project them onto the feature maps to extract point-wise features. The point-wise features corresponding to each point s in S_t are bilinearly sampled from $\phi_M^{t=1,2,3}$. (Note that $\phi_M^{t=0}$ is unnecessary here and is used as input for subsequent initialization.) Then the dimensions of these features

will be reduced by MLP(multi-layer perceptron) and concatenated as a feature vector $\hat{\phi}_M^t$ which can be formulated as:

$$\begin{aligned} \hat{\phi}_M^t &= \mathcal{F}(\phi_M^t, S_t) \\ &= \oplus \{f(\phi_M^t(s)), \text{ for } s \in S_t\}, \end{aligned} \quad (2)$$

where $\mathcal{F}(\cdot)$ denotes the overall point-wise feature extraction, $f(\cdot)$ is the MLP layer, and \oplus denotes the concatenation. We use an iterative mechanism to complete the interaction of different scale features. Sequentially, a parameter regressor \mathcal{R}_t takes features $\hat{\phi}_M^t$ and the current parameter estimation Θ_t as inputs and outputs the parameter residual. Parameters are updated as Θ_{t+1} by adding the residual to Θ_t which can be formulated as:

$$\Theta_{t+1} = \Theta_t + \mathcal{R}_t(\Theta_t, \hat{\phi}_M^t), \text{ for } t > 0. \quad (3)$$

The initial parameter Θ_0 is initialized by feeding $\phi_M^{t=0}$ into the regressor \mathcal{R}_t .

When the predicted parameters Θ (the subscript t is omitted for simplicity) are obtained through each scale feature, a mesh with vertices of $V = \mathcal{M}(\theta, \beta) \in \mathbb{R}^{N \times 3}$ can be generated accordingly, where $N = 6890$ is the number of vertices in the SMPL model. We downsample V to get the sampling point S_{t+1} for the next iteration. These mesh vertices can be mapped by pre-trained linear regressor to obtain sparse 3D keypoints $J \in \mathbb{R}^{N_j \times 3}$. With the estimated pseudo-camera parameters, we can obtain 2D keypoints $K \in \mathbb{R}^{N_j \times 2}$ by projecting J on the measurement coordinate system. We

calculate the loss between the 2D keypoints and the ground truth, in this way reducing the difference between the 2D projection and the human pose in the real scene. Concurrently, supplementary 3D supervisions regarding 3D keypoints and model parameters are integrated when authentic 3D labels are available. The total loss function for the parameter regressor is thereby formulated as follows:

$$\mathcal{L}_{\text{reg}} = \lambda_{2d} \|K - \hat{K}\|_2 + \lambda_{3d} \|J - \hat{J}\|_2 + \lambda_{\text{para}} \|\Theta - \hat{\Theta}\|_2, \quad (4)$$

where $\|\cdot\|_2$ is the squared L2 norm, \hat{K}, \hat{J} , and $\hat{\Theta}$ denote the ground truth 2D keypoints, 3D keypoints, and model parameters, respectively.

3.4. Double-Head Auxiliary Supervision

The spatial feature map of the human body is relatively rough and contains a lot of noise. Therefore, there are still some deviations in the perception of human limbs and pose. To improve our estimation accuracy of human limbs, we introduce a Double-Head Auxiliary Supervision (DHAS) mechanism to obtain finer spatial features during the training stage.

Specifically, we first convert all the spatial features at different scales to a single feature map ϕ^T by upsampling and then concatenating them together. The feature map ϕ^T is used for the different auxiliary supervision heads. On the one hand, we generate a heat map representation by a classification layer to explicitly indicate the position of the 2d keypoints. On the other hand, we also estimate a dense map through the IUV Predict layer to get a dense correspondence between the SMPL model and the feature map. The loss function for the Double-Head Auxiliary Supervision consists of two parts, which can be written as:

$$\mathcal{L}_{\text{das}} = \mathcal{L}_{\text{sc}} + \mathcal{L}_{\text{den}}. \quad (5)$$

Keypoints Supervision. We utilize the SimCC-based algorithm [24] for predicting pose keypoints. This approach treats keypoint localization as a classification task in horizontal and vertical coordinates. During training, instead of estimating the actual coordinates, we employ two vectors, x and y , and convert the ground truth 2D keypoints into such vectors to compute the loss. The loss function is then formulated as follows:

$$\mathcal{L}_{\text{sc}} = \lambda_{xy} (\text{KL-Loss}(x, \hat{x}) + \text{KL-Loss}(y, \hat{y})), \quad (6)$$

where KL-Loss is the Kullback-Leibler divergence loss, \hat{x} and \hat{y} denote the processed ground truth 2D keypoints, respectively.

IUV Supervision. We adopt the IUV mapping defined in DensePose [13] as the dense correspondence representation. This mapping establishes deterministic correspondences between foreground pixels in 2D images and vertices on 3D surfaces. The vertices on the template mesh can

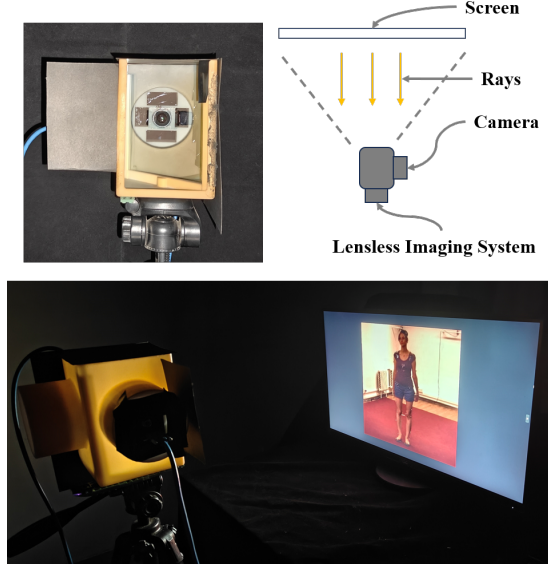


Figure 4. On the top left is a figure of the dual camera system we created. This system consists of an RGB camera and a lensless imaging system using a diffuser as a mask. The top right shows the process of collecting our dataset. The image at the bottom is a record of the process of collecting our dataset.

be mapped back to pixels on the foreground using a pre-defined bijection mapping between 3D surface space and 2D UV space. The dense correspondence representation comprises the index of body parts P and UV values of mesh vertices. During training, we apply classification loss to the index of body parts P and regression loss to the UV channels of the dense correspondence mapping. The loss function is formulated as follows:

$$\begin{aligned} \mathcal{L}_{\text{den}} = & \lambda_{pi} \text{CrossEntropy}(P, \hat{P}) \\ & + \lambda_{uv} \text{SmoothL1}(U, \hat{U}) \\ & + \lambda_{uv} \text{SmoothL1}(V, \hat{V}) \end{aligned} \quad (7)$$

where \hat{P}, \hat{U} , and \hat{V} denote the ground truth of P and UV values, respectively.

4. Experiments

4.1. Imaging System and Dataset

Lensless Imaging System. Due to the scarcity of human pose and shape datasets based on lensless imaging systems, we developed a basic lensless system to gather experimental data. The system, illustrated in Fig. 4, comprises two primary components: a lensless imaging system for capturing lensless measurements and an RGB camera for capturing real images corresponding to the lensless measurements. To ensure identical light paths, we employed a beam splitter between the lensless sensor and the RGB camera. This al-

lowed for consistent imaging conditions and facilitated accurate correlation between the lensless measurements and the corresponding real images.

For the lensless imaging part of the system, we adopted the Mask-Modulated Lensless System, inspired by design options such as diffusercam [2] and phlatcam [7]. Specifically, we selected a diffuser as our mask and incorporated PhlatCam’s concept of using larger sensors to enhance global information perception.

Datasets. The inputs to LPSNet are lensless measurements. However, datasets for classical human pose estimation are not directly available at present. Leveraging the lensless imaging system we have constructed, and the mathematical model of the system’s imaging, the sources of datasets for our experiments can be categorized as follows:

- **Real Dataset.** Using a lensless imaging system to capture images displayed on a screen as measurements is currently the primary method of acquiring datasets in the lensless field. We used this approach to collect datasets from various sources, including Human3.6M, MPII, COCO, 3DPW, and MIP-INF-3DHP datasets, which we refer to as LenslessHuman3.6M, LenslessMPII, LenslessMIP-INF-3DHP, LenslessCOCO, and Lensless3DPW, respectively. We also reclassified the training dataset and validation dataset on LenslessHuman3.6M, referred to as train-LenslessHuman3.6M and eval-LenslessHuman3.6M, respectively. Moreover, we capture the real scenes of different individuals, backgrounds, and light intensities using our lensless imaging system.
- **Simulated Dataset.** The mathematical imaging model enables the conversion (simulation) of images captured by RGB cameras into measurements captured by lensless imaging systems. This technique is commonly employed in lensless imaging fields for testing systems and imaging methods. Leveraging this, we converted numerous human pose datasets into simulated lensless measurements. These simulated datasets extended our training set and provided a quick validation of our method.

4.2. Implementation Details

The dimensions of the raw measurements are $1280 \times 1024 \times 3$. Prior to commencing the experiments, we first crop and resize the lensless measurements. These measurements are pre-processed to $224 \times 224 \times 3$ before being fed into the network. Following this pre-processing step, the lensless measurements inputted into the global perceptual layer are 224×224 , generating spatial features at resolutions of (7×7 , 14×14 , 28×28 , and 56×56). During the generation of mesh-aligned features, the SMPL mesh is down-sampled using a pre-computed downsampling matrix provided in [20], resulting in a reduction of vertex count from 6890 to 431. The regressors \mathcal{R}_t follow a congruent architec-

tural framework to the regressor present in HMR [16], albeit with slight variations in their input dimensions. Our network is trained using the Adam optimizer [17] with a learning rate of 5×10^{-5} and a batch size of 80 on 4 NVIDIA RTX2080 Ti GPUs. No learning rate decay is applied during training.

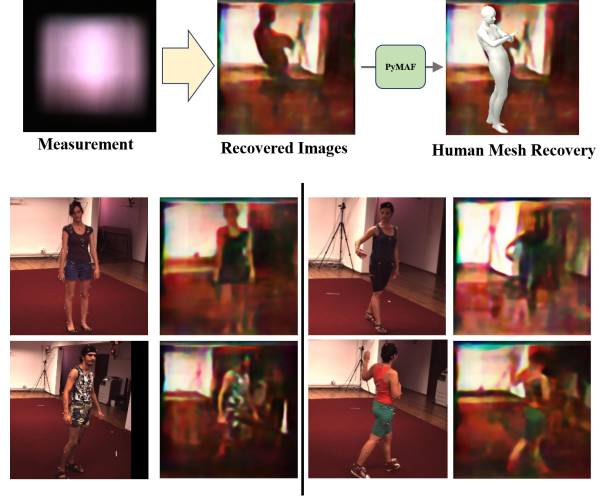


Figure 5. At the top is the frame of our baseline. Lensless measurements first recover the image by reconstruction methods and then estimate human pose and shape by PyMAF. The bottom image compares the recovered image with the original image, and we can see that the quality of the recovered image has dropped dramatically.

4.3. 3D Human Pose and Shape Comparison.

Baseline Approach. We are the first work to perform human pose and shape estimation through lensless measurements. Given the absence of other valid methods for comparison, we designed a baseline approach that approaches this as a two-stage task. The baseline architecture is depicted in Fig. 5. In the first stage, we utilized the lensless image reconstruction method Rego *et. al.* [30], chosen for its wide applicability in recovering images acquired by lensless imaging systems. In the second stage, PyMAF is used to estimate human pose and shape.

Method	MPJPE ↓	PA-MPJPE ↓	PVE ↓
baseline (PyMAF)	257.07	121.73	277.18
baseline (PyMAF [†])	126.28	81.37	151.60
LPSNet	119.20	81.52	134.74

Table 1. Comparison with baseline. The baseline is a combination of the two-stage approach using existing methods. LPSNet outperforms the baseline on the LenslessHuman3.6M datasets.

Comparison with Baseline. We present the results of

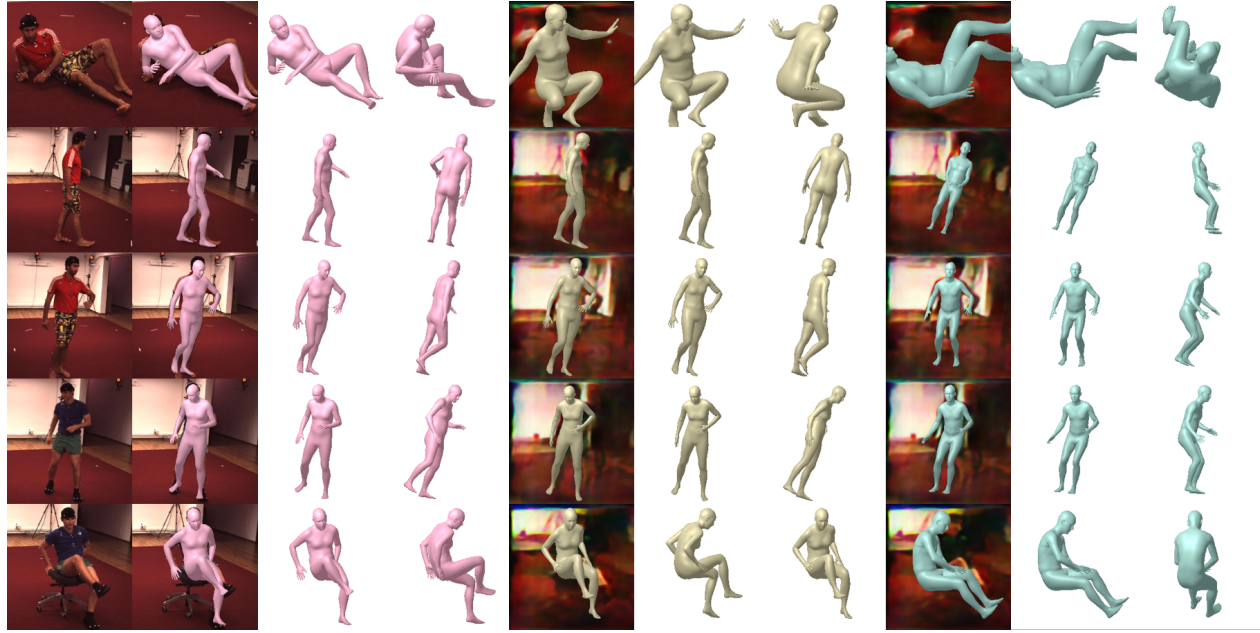


Figure 6. **Qualitative results of LPSNet on challenging LenslessHuman3.6M.** The results on the left are from our LPSNet estimation, those in the center are from our baseline (PyMAF) output, and those on the right are from the fine-tuned baseline (PyMAF \dagger) output. LPSNet can be seen to be better than the baselines.

the quantitative comparative evaluation on the LenslessHuman3.6M dataset in Tab. 1. Notably, images recovered from lensless measurements exhibit lower quality. Directly comparing the baseline (PyMAF) with our approach is challenging and unfair. Therefore, we fine-tuned PyMAF on the train-LenslessHuman3.6M dataset, denoted as PyMAF \dagger . Referring to Tab. 1, we observe significant improvements in the indicators of baseline(PyMAF \dagger). Specifically, compared with the baseline(PyMAF \dagger), the MPJPE of LPSNet on the LenslessHuman3.6M dataset is reduced by 7.08 mm.

As shown in Tab. 1, our LPSNet achieved competitive results compared to the baseline approach (PyMAF \dagger). LPSNet demonstrates more significant improvements in the MPJPE and PVE metrics. However, we would argue that the PA-MPJPE metric may not fully reveal the performance of the mesh-image alignment, as it is calculated as MPJPE after rigid alignment.

Baseline (PyMAF) has difficulty performing accurate pose estimation on low-quality recovered images. However, the outputs of our LPSNet exhibit significant improvements compared to the two baseline methods, especially for limb estimation. Qualitative comparison results are illustrated in Fig. 6.

4.4. Ablation Study

In this section, we conduct ablation studies on LenslessHuman3.6M under various settings to validate the effectiveness of the key components proposed in our method.

Method	MPJPE \downarrow	PA-MPJPE \downarrow	PVE \downarrow
w/o MSFDcoder and DHAS	142.13	92.20	161.07
w/o DHAS	139.34	92.56	158.97
w/o DHAS (2D keypoint)	123.30	83.41	138.67
w/o DHAS (IUV)	129.70	86.83	146.7
LPSNet	119.20	81.52	134.74

Table 2. Ablation study on LPSNet. DHAS stands for Double-Head Auxiliary Supervision.

All ablation variants were trained and tested on LenslessHuman3.6M, which is derived from the Human3.6M dataset. The Human3.6M dataset includes ground-truth 3D labels and serves as a widely used benchmark in 3D human pose and shape estimation.

Multi-Scale Lensless Feature Decoder. In LPSNet, the decoder primarily decodes the global information of lensless measurements encoded by the diffuser, which plays a crucial role in our end-to-end system. Our MSFDcoder is essential for efficient feature extraction from lensless measurements. We have adapted another variant of the decoder to verify this. Specifically, we simplified the global perception layer of the decoder to a series of convolutional layers and deconvolutional layers. We use this simpler decoder in the experiment(w/o MSFDcoder and DHAS) instead of MSFDcoder. As shown in Tab. 2, comparing the result of experiments(w/o MSFDcoder and DHAS) and experiment(w/o DHAS), we can see that MSFDcoder improves

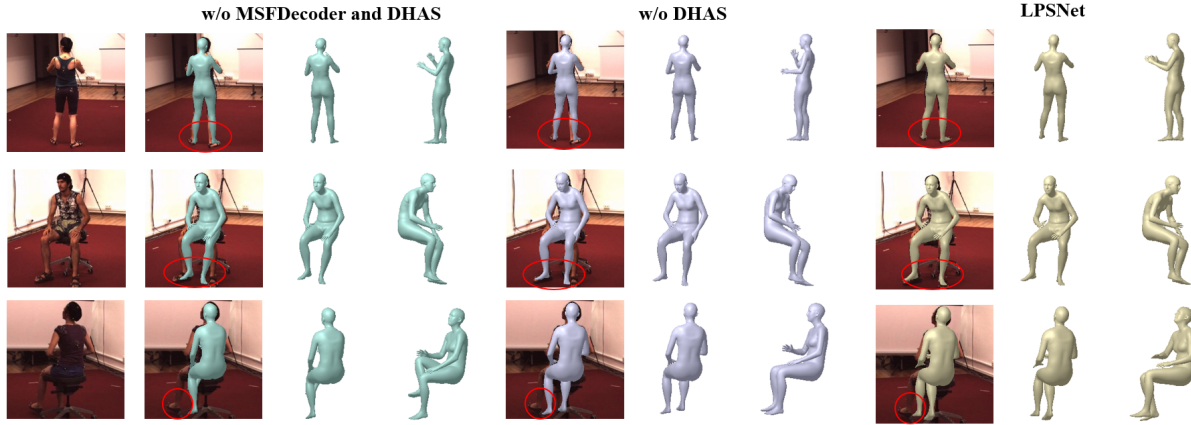


Figure 7. **Qualitative results of LPSNet on challenging LenslessHuman3.6M.** We can see that the results of LPSNet are better, and the results are improved with the addition of the double-head assisted supervision mechanism.

the accuracy of the human pose and shape estimation significantly. Through the qualitative experiment in Fig. 7, we can also see that the human pose and shape estimation has a better alignment after using the MSFDecoder. Note that neither experiment(w/o MSFDcoder and DHAS) nor the experiment(w/o DHAS) used auxiliary supervision.

Double-Head Auxiliary Supervision. Double-Head Auxiliary Supervision is mainly used to improve the accuracy of human limbs. For each auxiliary supervisory head, we conducted ablation experiments respectively. Referring to the result in Tab. 2, LPSNet has significant improvements in the MPJPE and the PVE metrics. Fig. 7 shows additional qualitative comparison results. We can see that the alignment of the human pose and shape is better with the addition of the Double-Head Auxiliary Supervision mechanism.

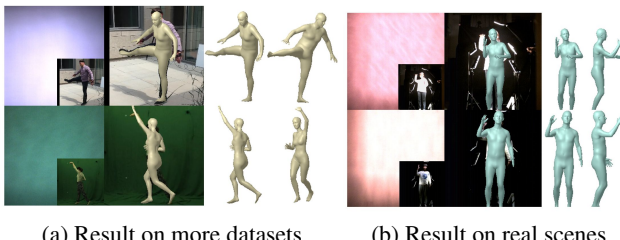


Figure 8. Results on more datasets and real scenes. From left to right for each set of figures: lensless measurement, alignment of results with RGB images, and 3D results shown in different views.

4.5. Results on more Datasets and Real Scene

Fig. 8 (a) shows the qualitative results on various datasets after using the mixed datasets for training. Specifically, we collected the MPII, COCO, 3DPW, MIP-INF-3DHP, and LSP datasets through our lensless imaging system and mixed them for training and testing.

In addition, we also capture the real scenes of two different people, in different backgrounds and different light intensities using our lensless imaging system. Fig. 8 (b) illustrates the experimental results of our method on these real scenes, indicating its suitability for real-world applications.

5. Conclusion and Discussion

Conclusion. In this paper, we propose the first end-to-end framework to recover 3D human poses and shapes from lensless measurements to the best of our knowledge. Specifically, we design a multi-scale lensless feature decoder, which can effectively decode the information produced by the lensless imaging system. We also propose a double auxiliary supervision mechanism to improve the accuracy of human limb end estimation. Experimental results show that our method can achieve end-to-end human pose and shape estimation through lensless measurements.

Limitations and Future Work. Our work is an initial stride step in this direction, however, the results are still not as robust as those achieved by traditional methods for estimating the human body from RGB images. The current scarcity of lensless datasets hampers our ability to pre-train the MSFDecoder using a large dataset like ImageNet [9], thereby limiting the generalizability of our approach. We will continue this work in the future, focusing on generating more extensive lensless datasets and progressing towards practical applications.

Acknowledgments. This work was supported in part by the National Key R&D Program of China (2023YFC3082100), the National Natural Science Foundation of China (62122058 and 62171317), and the Science Fund for Distinguished Young Scholars of Tianjin (No. 22JCJQJC00040).

References

- [1] Jesse K Adams, Vivek Boominathan, Benjamin W Avants, Daniel G Vercosa, Fan Ye, Richard G Baraniuk, Jacob T Robinson, and Ashok Veeraraghavan. Single-Frame 3D Fluorescence Microscopy with Ultraminiature Lensless FlatScope. *Sci Adv.*, 3(12):e1701548, 2017. [2](#)
- [2] Nick Antipa, Grace Kuo, Reinhard Heckel, Ben Mildenhall, Emrah Bostan, Ren Ng, and Laura Waller. DiffuserCam: Lensless Single-exposure 3D Imaging. *Optica*, 5(1):1–9, 2018. [2, 6](#)
- [3] Anurag Arnab, Carl Doersch, and Andrew Zisserman. Exploiting Temporal Context for 3D Human Pose Estimation in theild. In *IEEE Conf. Comput. Vis. Pattern Recog.*, pages 3395–3404, 2019. [3](#)
- [4] M Salman Asif, Ali Ayremlou, Aswin Sankaranarayanan, Ashok Veeraraghavan, and Richard G Baraniuk. Flatcam: Thin, Lensless Cameras using Coded Aperture and Computation. *IEEE Trans Comput Imaging.*, 3(3):384–397, 2016. [2](#)
- [5] Federica Bogo, Angjoo Kanazawa, Christoph Lassner, Peter Gehler, Javier Romero, and Michael J. Black. Keep it SMPL: Automatic Estimation of 3D Human Pose and Shape from a Single Image. In *Eur. Conf. Comput. Vis.* Springer International Publishing, 2016. [3](#)
- [6] Vivek Boominathan, Jesse K Adams, M Salman Asif, Benjamin W Avants, Jacob T Robinson, Richard G Baraniuk, Aswin C Sankaranarayanan, and Ashok Veeraraghavan. Lensless Imaging: A Computational Renaissance. *IEEE Signal Process Mag.*, 33(5):23–35, 2016. [1](#)
- [7] Vivek Boominathan, Jesse K Adams, Jacob T Robinson, and Ashok Veeraraghavan. Phlatcam: Designed Phase-Mask Based Thin Lensless Camera. *IEEE Trans. Pattern Anal. Mach. Intell.*, 42(7):1618–1629, 2020. [1, 2, 6](#)
- [8] Junhyeong Cho, Kim Youwang, and Tae-Hyun Oh. Cross-attention of disentangled modalities for 3d human mesh recovery with transformers. In *Eur. Conf. Comput. Vis.*, pages 342–359. Springer, 2022. [3](#)
- [9] J. Deng, W. Dong, R. Socher, L. Li, Kai Li, and Li Fei-Fei. Imagenet: A large-scale hierarchical image database. In *IEEE Conf. Comput. Vis. Pattern Recog. Workshops (CVPR Workshops)*. [8](#)
- [10] Georgios Georgakis, Ren Li, Srikrishna Karanam, Terrence Chen, Jana Košeká, and Ziyan Wu. Hierarchical Kinematic Human Mesh Recovery. In *Eur. Conf. Comput. Vis.*, pages 768–784. Springer, 2020. [3](#)
- [11] Shubham Goel, Georgios Pavlakos, Jathushan Rajasegaran, Angjoo Kanazawa, and Jitendra Malik. Humans in 4D: Reconstructing and Tracking Humans with Transformers. In *Int. Conf. Comput. Vis.*, pages 14783–14794, 2023. [1, 3](#)
- [12] Joseph W Goodman. *Introduction to Fourier optics*. Roberts and Company publishers, 2005.
- [13] Rıza Alp Güler, Natalia Neverova, and Iasonas Kokkinos. Densepose: Dense Human Pose Estimation in the Wild. In *Int. Conf. Comput. Vis.*, pages 7297–7306, 2018. [5](#)
- [14] Catalin Ionescu, Dragos Papava, Vlad Olaru, and Cristian Sminchisescu. Human3. 6M: Large Scale Datasets and Predictive Methods for 3D Human Sensing in Natural Environ- ments. *IEEE Trans. Pattern Anal. Mach. Intell.*, 36(7):1325–1339, 2013.
- [15] Hanbyul Joo, Natalia Neverova, and Andrea Vedaldi. Exemplar Fine-Tuning for 3D Human Model Fitting Towards In-the-Wild 3D Human Pose Estimation. In *Int. Conf. 3D. Vis.*, pages 42–52. IEEE, 2021. [3](#)
- [16] Angjoo Kanazawa, Michael J. Black, David W. Jacobs, and Jitendra Malik. End-to-end Recovery of Human Shape and Pose. In *IEEE Conf. Comput. Vis. Pattern Recog.*, 2018. [1, 3, 4, 6](#)
- [17] Diederik P Kingma and Jimmy Ba. Adam: A method for stochastic optimization. *arXiv preprint arXiv:1412.6980*, 2014. [6](#)
- [18] Muhammed Kocabas, Chun-Hao P Huang, Otmar Hilliges, and Michael J Black. PARE: Part Attention Regressor for 3D Human Body Estimation. In *Int. Conf. Comput. Vis.*, pages 11127–11137, 2021. [3](#)
- [19] Nikos Kolotouros, Georgios Pavlakos, Michael J Black, and Kostas Daniilidis. Learning to Reconstruct 3D Human Pose and Shape Via Model-fitting in the Loop. In *Int. Conf. Comput. Vis.*, pages 2252–2261, 2019. [3](#)
- [20] Nikos Kolotouros, Georgios Pavlakos, and Kostas Daniilidis. Convolutional Mesh Regression for Single-Image Human Shape Reconstruction. In *IEEE Conf. Comput. Vis. Pattern Recog.*, pages 4501–4510, 2019. [3, 6](#)
- [21] Grace Kuo, Nick Antipa, Ren Ng, and Laura Waller. DiffuserCam: Diffuser-Based Lensless Cameras. In *Computational Optical Sensing and Imaging*, pages CTu3B–2. Optica Publishing Group, 2017. [1, 2](#)
- [22] Christoph Lassner, Javier Romero, Martin Kiefel, Federica Bogo, Michael J. Black, and Peter V. Gehler. Unite the People: Closing the Loop Between 3D and 2D Human Representations. In *IEEE Conf. Comput. Vis. Pattern Recog.*, 2017. [3](#)
- [23] Vincent Leroy, Philippe Weinzaepfel, Romain Brégier, Hadrien Combaluzier, and Grégory Rogez. SMPLy Benchmarking 3D Human Pose Estimation in the wild. In *Int. Conf. 3D. Vis.*, pages 301–310. IEEE, 2020. [3](#)
- [24] Yanjie Li, Sen Yang, Peidong Liu, Shoukui Zhang, Yunxiao Wang, Zhicheng Wang, Wankou Yang, and Shu-Tao Xia. SimCC: A Simple Coordinate Classification Perspective for Human Pose Estimation. In *Eur. Conf. Comput. Vis.*, pages 89–106. Springer, 2022. [5](#)
- [25] Kevin Lin, Lijuan Wang, and Zicheng Liu. End-to-end human pose and mesh reconstruction with transformers. In *IEEE Conf. Comput. Vis. Pattern Recog.*, pages 1954–1963, 2021. [3](#)
- [26] Kevin Lin, Lijuan Wang, and Zicheng Liu. Mesh Graphomer. In *Int. Conf. Comput. Vis.*, pages 12939–12948, 2021. [3](#)
- [27] Aydogan Ozcan and Euan McLeod. Lensless Imaging and Sensing. *Annual review of biomedical engineering*, 18:77–102, 2016. [1](#)
- [28] Georgios Pavlakos, Vasileios Choutas, Nima Ghorbani, Timo Bolkart, Ahmed A. A. Osman, Dimitrios Tzionas, and Michael J. Black. Expressive Body Capture: 3D Hands, Face, and Body from a Single Image. In *IEEE Conf. Comput. Vis. Pattern Recog.*, 2019. [3](#)

- [29] Georgios Pavlakos, Jitendra Malik, and Angjoo Kanazawa. Human Mesh Recovery from Multiple Shots. In *IEEE Conf. Comput. Vis. Pattern Recog.*, pages 1485–1495, 2022. 3
- [30] Joshua D Rego, Karthik Kulkarni, and Suren Jayasuriya. Robust Lensless Image Reconstruction Via PSF Estimation. In *Proceedings of the IEEE/CVF Winter Conference on Applications of Computer Vision*, pages 403–412, 2021. 6
- [31] Davis Rempe, Tolga Birdal, Aaron Hertzmann, Jimei Yang, Srinath Sridhar, and Leonidas J. Guibas. HuMoR: 3D Human Motion Model for Robust Pose Estimation. In *Int. Conf. Comput. Vis.*, 2021. 3
- [32] David G Stork and Patrick R Gill. Lensless Ultra-miniature CMOS Computational Imagers and Sensors. *Proc. Sensor-comm*, pages 186–190, 2013. 2
- [33] David G Stork and Patrick R Gill. Optical, mathematical, and computational foundations of lensless ultra-miniature diffractive imagers and sensors. *International Journal on Advances in Systems and Measurements*, 7(3):4, 2014. 2
- [34] Ke Sun, Bin Xiao, Dong Liu, and Jingdong Wang. Deep High-resolution Representation Learning for Human Pose Estimation. In *IEEE Conf. Comput. Vis. Pattern Recog.*, pages 5693–5703, 2019. 3
- [35] Garvita Tiwari, Dimitrije Antic, Jan Eric Lenssen, Niko-laos Sarafianos, Tony Tung, and Gerard Pons-Moll. Pose-NDF: Modeling Human Pose Manifolds with Neural Distance Fields. In *Eur. Conf. Comput. Vis.*, 2022. 3
- [36] Hongwen Zhang, Jie Cao, Guo Lu, Wanli Ouyang, and Zhenan Sun. Learning 3D Human Shape and Pose from Dense Body Parts. *IEEE Trans. Pattern Anal. Mach. Intell.*, 44(5):2610–2627, 2020. 1
- [37] Hongwen Zhang, Yating Tian, Xinchi Zhou, Wanli Ouyang, Yebin Liu, Limin Wang, and Zhenan Sun. Pymaf: 3d human pose and shape regression with pyramidal mesh alignment feedback loop. In *Int. Conf. Comput. Vis.*, pages 11446–11456, 2021. 1, 3, 4
- [38] Jason Y Zhang, Panna Felsen, Angjoo Kanazawa, and Jitendra Malik. Predicting 3D Human Dynamics from Video. In *Int. Conf. Comput. Vis.*, pages 7114–7123, 2019. 3

Supplementary Document for LPSNet: End-to-End Human Pose and Shape Estimation with Lensless Imaging

Haoyang Ge^{1,†}, Qiao Feng^{1,†}, Hailong Jia¹, Xiongzheng Li¹, Xiangjun Yin¹,

You Zhou², Jingyu Yang¹, Kun Li^{1,*}

¹Tianjin University, China ²Nanjing University, China

`{ghy0623, fengqiao, jhl, lxz, yinxiangjun, yjy, lik}@tju.edu.cn zhouyou@nju.edu.cn`

In this document, we provide the following supplementary contents:

- Training Loss;
- Evaluation;
- Experimental Results on Simulated Dataset;
- Failure Cases and Limitations.

We also provide a demo video on our [project page](#).

1. Training Loss

We introduce multiple training losses as supervision for LPSNet: the reconstruction loss, the Kullback-Leibler divergence loss, and the environmental constraint loss. Formally, the entire training loss is formulated as follows:

$$\mathcal{L} = \mathcal{L}_{\text{reg}} + \mathcal{L}_{\text{das}}. \quad (1)$$

- **Regressor Loss** \mathcal{L}_{reg} . This loss is formulated as:

$$\mathcal{L}_{\text{reg}} = \lambda_{2D} \mathcal{L}_{2D} + \lambda_{3D} \mathcal{L}_{3D} + \lambda_{\text{para}} \mathcal{L}_{\text{para}}, \quad (2)$$

where \mathcal{L}_{2D} , \mathcal{L}_{3D} and $\lambda_{\text{para}} \mathcal{L}_{\text{para}}$ denote the 2D keypoints loss, the 3D keypoints loss and the SMPL parameter reconstruction loss, respectively.

- **Double-Head Auxiliary Supervision Loss** \mathcal{L}_{das} . This loss is formulated as:

$$\mathcal{L}_{\text{das}} = \mathcal{L}_{\text{sc}} + \mathcal{L}_{\text{den}}, \quad (3)$$

where \mathcal{L}_{sc} and \mathcal{L}_{den} denote the IUV Supervision loss and Keypoints Supervision loss:

$$\mathcal{L}_{\text{sc}} = \lambda_{xy} (\text{KL-Loss}(x, \hat{x}) + \text{KL-Loss}(y, \hat{y})), \quad (4)$$

$$\begin{aligned} \mathcal{L}_{\text{den}} &= \lambda_{pi} \text{CrossEntropy}(P, \hat{P}) \\ &+ \lambda_{uv} \text{SmoothL1}(U, \hat{U}) \\ &+ \lambda_{uv} \text{SmoothL1}(V, \hat{V}). \end{aligned} \quad (5)$$

2. Evaluation Metrics

Here, we describe the evaluation metrics we used in our experiments. First, we report the widely used MPJPE (mean per joint position error), which is calculated as the mean of the Euclidean distances between the ground truth and the predicted joint positions after centering the pelvis joint on the ground truth location (as is common practice):

$$MPJPE = \frac{1}{N} \sum_{i=1}^N \|p_i - q_i\|_2. \quad (6)$$

Also, we report PA-MPJPE (Procrustes Aligned MPJPE), which is calculated similarly to MPJPE but after a rigid alignment of the predicted pose to the ground truth pose,

$$PA - MPJPE = \frac{1}{N} \sum_{i=1}^N \|p_i - q_i\|_2. \quad (7)$$

Furthermore, we calculate Per-Vertex-Error (PVE), which is denoted by the Euclidean distance between the ground truth and predicted mesh vertices that are the output of SMPL layer:

$$PVE = \frac{1}{M} \sum_{j=1}^M \|v_j - w_j\|_2. \quad (8)$$

3. Experimental Results on Simulated Dataset

We also create a simulation dataset; through the simulation dataset, the feasibility of our experiment can be further verified. We create a simulation application based on the principle of lensless imaging to model the imaging process of lensless imaging. We design the simulation application by referring to the imaging model of PhlatCam [1]. A real-world 2D scene $i(x, y; z)$ at a distance z can be assumed to be made up of incoherent point sources. Each point source will produce a shifted version of PSF $p_z(x, y)$, and since the sources are incoherent to each other, the shifted PSF will

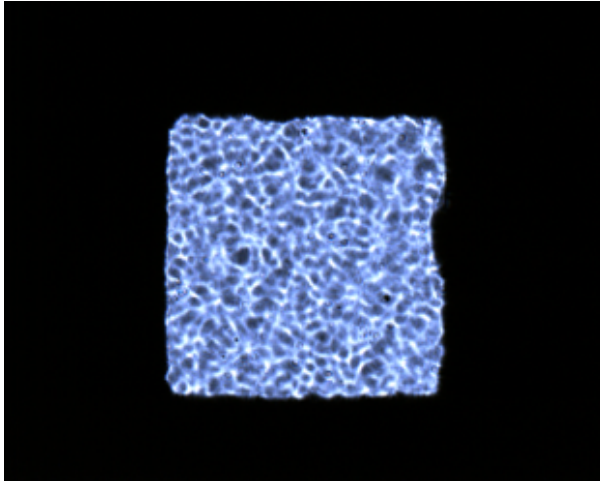


Figure 1. The PSF acquired by our imaging system.

add linearly in intensity [2] at the sensor. By Property 1 of the PSF, we can write the imaging model as the following convolution model:

$$\mathbf{b}(x, y) = p_z(x, y) * \mathbf{i}(x, y; z). \quad (9)$$

Here, \mathbf{b} is the sensor's capture, and $*$ denotes 2D convolution over (x, y) . We capture the PSF of our system as shown in Fig. 1, and we use the PSF and the existing human posture dataset to get the simulation dataset based on the imaging modality. We perform simulations on the Human3.6M dataset [3]. Fig. 2 and Fig. 3 show the results of LPSNet on the simulated dataset.

4. Failure Cases and Limitations

There are some limitations and some difficult cases that we have not solved very well. Fig. 4, Fig. 5, Fig. 6 shows, some failure cases of our approach. When human movement is more complex, the human pose and shape, as estimated by LPSNet, will have a large deviation. As shown in Fig. 5, the error in human pose and shape estimation also becomes larger when the human body is obscured.

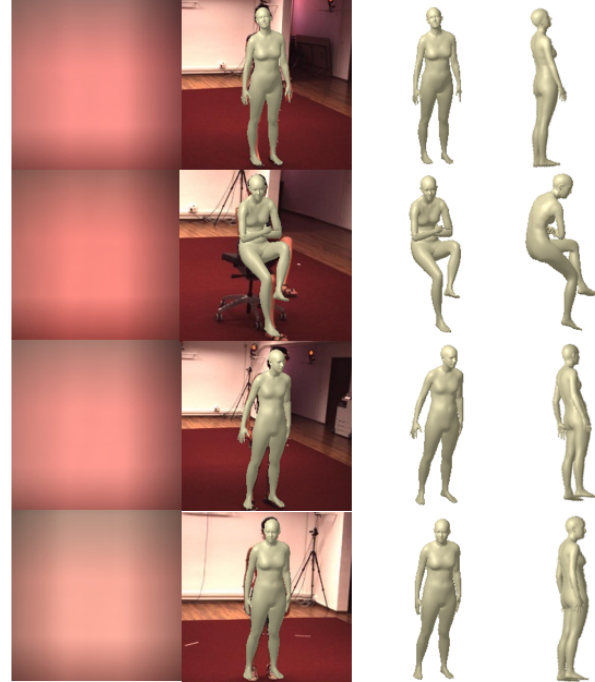


Figure 2. From left to right: lensless measurements, alignment of the estimated body mesh with the original scene, and reconstruction results of LPSNet on the simulated dataset.

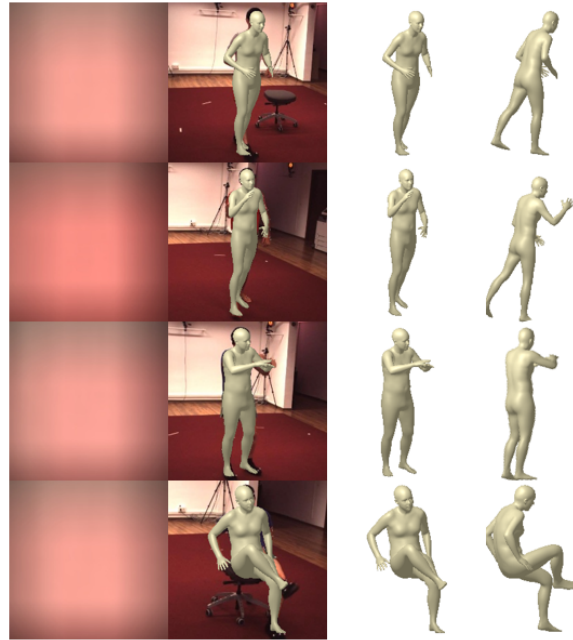


Figure 3. From left to right: lensless measurements, alignment of the estimated body mesh with the original scene, reconstruction results of LPSNet on the simulated dataset.

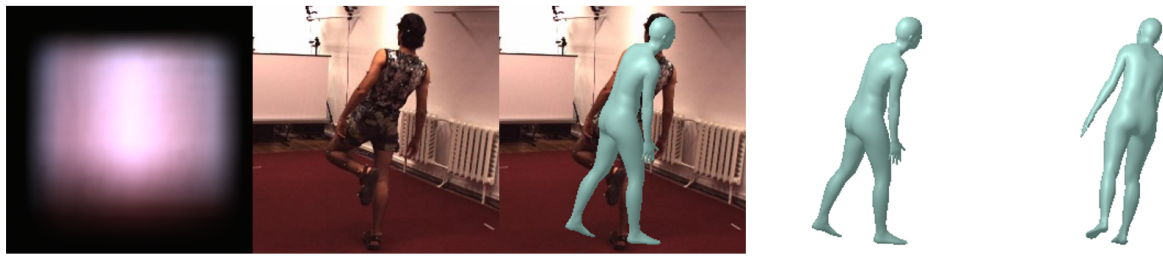


Figure 4. **Failure results for LPSNet.** From left to right: lensless measurements, real scene, alignment of the estimated body mesh with the original scene, reconstruction results of LPSNet. The poses of the characters in the scene are more complex and difficult to reconstruct.

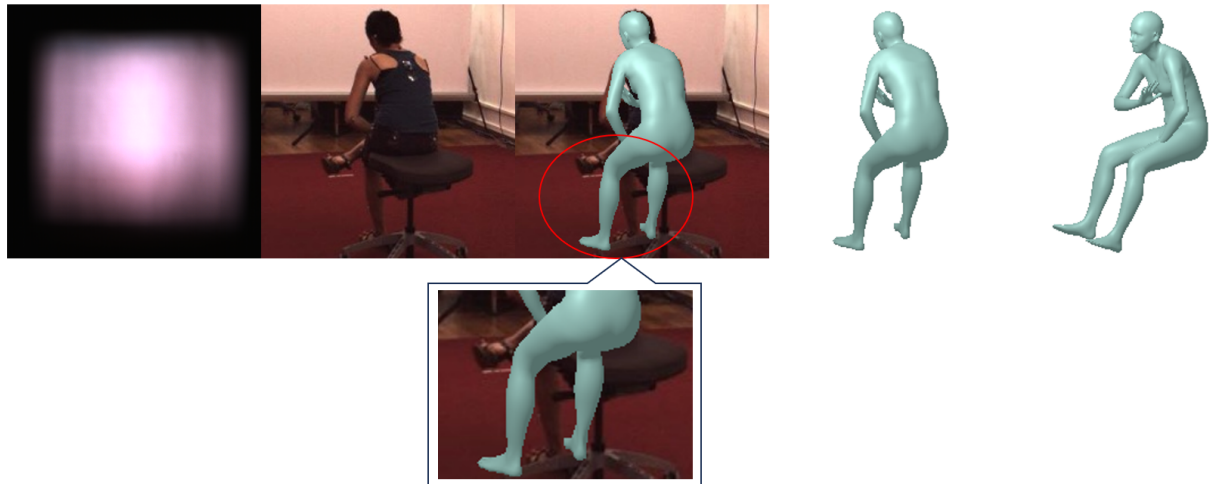


Figure 5. **Failure results for LPSNet.** From left to right: lensless measurements, real scene, alignment of the estimated body mesh with the original scene, reconstruction results of LPSNet. The enlarged image shows that the reconstruction of the obscured part fails.

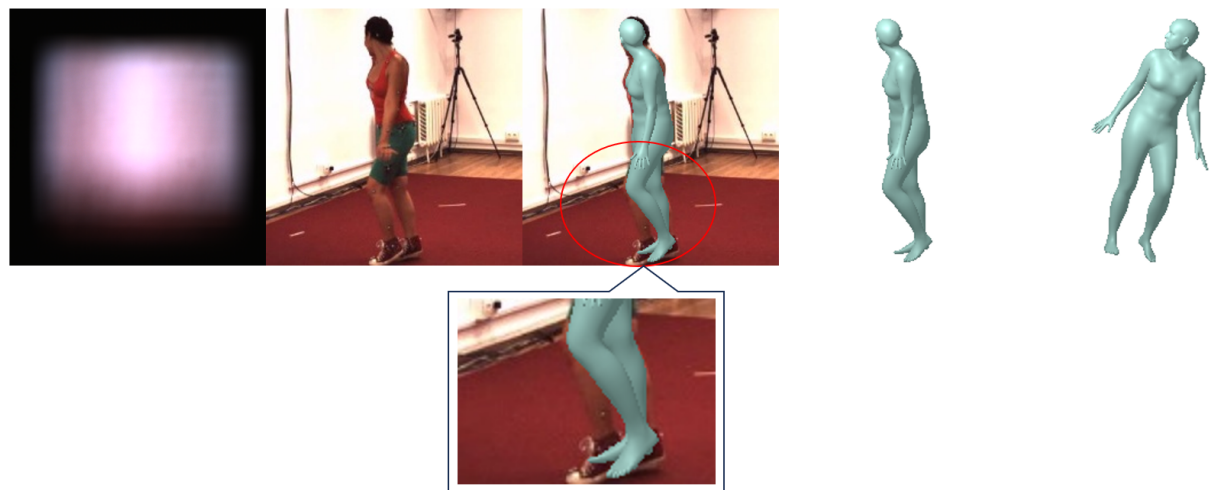


Figure 6. **Failure results for LPSNet.** From left to right: lensless measurements, real scene, alignment of the estimated body mesh with the original scene, reconstruction results of LPSNet. Poses overlap heavily with large reconstruction errors.

References

- [1] Vivek Boominathan, Jesse K Adams, Jacob T Robinson, and Ashok Veeraraghavan. Phlatcam: Designed Phase-Mask Based Thin Lensless Camera. *IEEE Trans. Pattern Anal. Mach. Intell.*, 42(7):1618–1629, 2020. [1](#)
- [2] Joseph W Goodman. *Introduction to Fourier optics*. Roberts and Company publishers, 2005. [2](#)
- [3] Catalin Ionescu, Dragos Papava, Vlad Olaru, and Cristian Sminchisescu. Human3. 6M: Large Scale Datasets and Predictive Methods for 3D Human Sensing in Natural Environments. *IEEE Trans. Pattern Anal. Mach. Intell.*, 36(7):1325–1339, 2013. [2](#)